

BAYESIAN MASS ESTIMATES OF THE MILKY WAY:
INCLUDING MEASUREMENT UNCERTAINTIES WITH HIERARCHICAL BAYES

GWENDOLYN M. EADIE¹, AARON SPRINGFORD², AND WILLIAM E. HARRIS¹

¹Dept. of Physics & Astronomy, McMaster University, Hamilton, ON L8S 4M1, Canada.

²Dept. of Mathematics & Statistics, Queen’s University, Kingston, ON K7L 3N6, Canada.

ABSTRACT

We present a hierarchical Bayesian method for estimating the total mass and mass profile of the Milky Way Galaxy. The new hierarchical Bayesian approach further improves the framework presented by Eadie et al. (2015b); Eadie & Harris (2016) and builds upon the preliminary reports by Eadie et al. (2015a,c). The method uses a distribution function $f(\mathcal{E}, L)$ to model the galaxy and kinematic data from satellite objects such as globular clusters to trace the Galaxy’s gravitational potential. A major advantage of the method is that it not only includes complete and incomplete data simultaneously in the analysis, but also incorporates measurement uncertainties in a coherent and meaningful way. We first test the hierarchical Bayesian framework, which includes measurement uncertainties, using the same data and power-law model assumed in Eadie & Harris (2016), and find the results are similar but more strongly constrained. Next, we take advantage of the new statistical framework and incorporate all possible globular cluster data, finding a cumulative mass profile with Bayesian credible regions. This profile implies a mass within 125kpc of $4.81 \times 10^{11} M_{\odot}$ with a 95% Bayesian credible region of $(3.96 - 5.76) \times 10^{11} M_{\odot}$.

Keywords: Galaxy: halo — Galaxy: kinematics and dynamics — Galaxy: general — dark matter — methods: statistical — globular clusters: general

1. INTRODUCTION

In our two previous papers, Eadie et al. (2015b, hereafter Paper I) and Eadie & Harris (2016, in press, accepted to ApJ, hereafter Paper II), we estimated the Galaxy’s mass and mass profile using a new Bayesian method and the kinematic data of Milky Way globular clusters (GCs) and dwarf galaxies (DGs). Paper I laid the groundwork; we tested the method on simulated data and then applied the method to Milky Way satellite data in a preliminary analysis. A main advantage of the new Bayesian method is that both complete and incomplete velocity vectors are included in the analysis simultaneously. Furthermore, the tests on simulated data showed that Galactic mass estimates are insensitive to misspecified velocity anisotropy assumptions. Paper I incorporated an analytic Hernquist model (for simplicity and testing of the method), and used GCs and DGs as tracers of the Milky Way’s potential. An assumption was that the satellites followed the same spatial distribution as the dark matter. Despite the simplicity of the model, the results were in agreement with many other studies (see Wang et al. 2015, for a comparison figure).

The promising results of Paper I led us to implement an arguably more realistic model for the Milky Way in Paper II, in which the distribution of the dark matter and the Galactic tracers are allowed to differ. The Paper II model uses power-law profiles with different parameters for the dark matter and tracers, and also includes velocity anisotropy as a parameter. This model is explained in detail by Evans et al. (1997), and previous applications of the model to the Milky Way and other galaxies were completed by Deason et al. (2011, 2012a,b, note that the notations between Evans’ and Deason’s papers differ).

Because the model includes a spatial profile for only a single population of tracers, we used GC kinematic data alone instead of a mixture of DGs and GCs. The results in Paper II suggested a significantly lower mass estimate for the Milky Way dark matter halo than we found in Paper I under the Hernquist model. The new results were closer in agreement to recent studies which suggest a “light” Milky Way (e.g. Gibbons et al. 2014).

An issue that is not fully addressed in Paper I or II is the inclusion of measurement uncertainty. Measurement uncertainties can differ substantially from object to object, with some tracers having very precise measurements and others having very imprecise ones. When

these uncertainties are not taken into account, then all of the data are treated as equally reliable.

This assumption of equal reliability can substantially affect the analysis when measurement uncertainties differ. For instance, a satellite that has an extreme velocity measurement might simply have a large measurement error, or it might actually have an extreme velocity. Our estimation of which of these cases is more likely depends on our knowledge of the measurement uncertainty. The interpretation of this satellite under any model should therefore depend how certain we are of its measured attributes.

Using a sensitivity analysis, Paper I showed that measurement uncertainties can play a significant role in the mass estimate of the Galaxy, contributing up to 50% of the uncertainty in the estimate. In addition, we found that certain measurements had very high leverage. For example, when the single GC Palomar 3 was removed from the analysis, the mass estimate of the Galaxy decreased by more than 12%. Thus, including measurement uncertainties would make a significant improvement to the analysis method described in Eadie et al. (2015b) and Eadie & Harris (2016).

Here, we substantially improve upon Paper II by introducing a *hierarchical* Bayesian method that includes the measurement uncertainties of proper motions and line-of-sight velocities in a measurement model. Preliminary tests of this method have already been reported by Eadie, Harris, Widrow, & Springford (2015c) and Eadie, Harris, & Springford (2015a) using the Hernquist model and data from GCs and DGs in Paper I, but here we apply the arguably more realistic tracer model from Paper II, and also use all of the available GC data.

2. METHOD

The method presented here builds on the work by Eadie et al. (2015b) (Paper I) and Eadie & Harris (2016) (Paper II), and the methods contained therein.

In Papers I and II, we defined the posterior distribution from Bayes' theorem as $p(\boldsymbol{\theta}|\mathbf{y})$, where $\boldsymbol{\theta}$ is the vector of model parameters, and \mathbf{y} is the vector of data. In practice, the posterior distribution is difficult to calculate directly, and MCMC methods are used to sample a distribution that is proportional to the posterior distribution. Assuming conditional independence of the $\{\mathbf{y}\}$, we write this distribution as

$$p(\boldsymbol{\theta}|\mathbf{y}) \propto \prod_i^n p(y_i|\boldsymbol{\theta}) p(\boldsymbol{\theta}) \quad (1)$$

$$= \prod_i^n p((r_i, v_{r,i}, v_{t,i})|\boldsymbol{\theta}) p(\boldsymbol{\theta}). \quad (2)$$

Above, r_i , $v_{r,i}$, and $v_{t,i}$ represent the Galactocentric distance, radial velocity, and tangential velocity of the i^{th}

tracer (GC). We assume that the GC positions and velocities are independent of one another, conditional on the value of $\boldsymbol{\theta}$.

In Paper II, we defined $p((r_i, v_{r,i}, v_{t,i})|\boldsymbol{\theta})$ by the *distribution function* (DF)

$$f(\mathcal{E}, L) = \frac{L^{-2\beta} \mathcal{E}^{\frac{\beta(\gamma-2)}{\gamma} + \frac{\alpha}{\gamma} - \frac{3}{2}}}{\sqrt{8\pi^3} 2^{-2\beta} \Phi_o^{-\frac{2\beta}{\gamma} + \frac{\alpha}{\gamma}}} \frac{\Gamma\left(\frac{\alpha}{\gamma} - \frac{2\beta}{\gamma} + 1\right)}{\Gamma\left(\frac{\beta(\gamma-2)}{\gamma} + \frac{\alpha}{\gamma} - \frac{1}{2}\right)}. \quad (3)$$

where $\mathcal{E} = -v^2/2 + \Phi(r)$, $L = rv_t$, and the model parameters are $\boldsymbol{\theta} = (\Phi_o, \gamma, \alpha, \beta)$ (beware of notational differences between papers Evans et al. 1997; Deason et al. 2011, 2012a,b). Under this definition, all stochasticity in $\{r_i, v_{r,i}, v_{t,i}\}$ is due to the actual positions and velocities of tracers in the Milky Way, and our particular realization of the Galaxy merely provides a sample of tracer kinematics. In Papers I and II, the measured values of $\{r_i, v_{r,i}, v_{t,i}\}$ are assumed to be the true values, which we condition upon to obtain the posterior distribution for $\boldsymbol{\theta}$.

The DF (Equation 3) is found by assuming that the dark matter halo follows a power-law profile of $\Phi(r) = \frac{\Phi_o}{r^\gamma}$, and that the spatial number density profile of the tracers follows $\rho(r) \propto r^{-\alpha}$. The parameter β is the standard anisotropy parameter, where the limits $\beta = 1$ and $\beta \rightarrow -\infty$ correspond to completely radial or completely tangential orbital distributions for the tracers (Binney & Tremaine 2008). The DF in eq. 3 assumes a spherical and non-rotating system, and also requires that $\mathcal{E} > 0$ (i.e. that tracers are bound to the Galaxy). Under this model, the mass profile of the dark matter halo is,

$$M(r) = \frac{\gamma\Phi_o}{G} \left(\frac{r}{\text{kpc}}\right)^{1-\gamma} \quad (4)$$

(Deason et al. 2012b), which has the physical limits of an isothermal sphere ($\gamma \rightarrow 0$) and a central point mass ($\gamma \rightarrow 1$).

The DF in eq. 3 is written in the Galactocentric reference frame—the frame in which the geometry of the model is the most straight-forward. The GC kinematic measurements and their uncertainties, on the other hand, are taken in the Heliocentric reference frame. Although the mathematical transformation of velocity and position vectors from a Heliocentric frame to a Galactocentric frame is relatively straightforward, transforming *uncertainties* from one frame to the other is a daunting task that requires complex error propagation which is non-linear, and that likely results in non-Gaussian errors. Therefore, we employ a different approach to incorporating the measurement uncertainties using a hierarchical Bayesian model.

2.1. Hierarchical Bayesian Model

The approach starts with a slight change in perspective: instead of treating the measurements of position r , line-of-sight velocity v_{los} , and proper motions in RA ($\mu_\alpha \cos \delta$) and DEC (μ_δ) as the *true* values, we treat these measurements as samples drawn from a distribution which depends on the true values. That is, the true values are now included as parameters in the model. For a given GC, the true position and velocity components are denoted in **blue** as the parameters,

$$\boldsymbol{\vartheta} = (r, v_{los}, \mu_\delta, \mu_\alpha \cos \delta), \quad (5)$$

the *measurements* are denoted in **black** as

$$\mathbf{y} = (r, v_{los}, \mu_\delta, \mu_\alpha \cos \delta), \quad (6)$$

and the measurement *uncertainties* are denoted in **red** as

$$\boldsymbol{\Delta} = (\Delta r, \Delta v_{los}, \Delta \mu_\delta, \Delta \mu_\alpha \cos \delta). \quad (7)$$

We assume that the measurements are samples drawn from Gaussian (also known as Normal) distributions centered around $\boldsymbol{\vartheta}$, and the measurement uncertainties $\boldsymbol{\Delta}$ are taken to be standard deviations. For example, the measurement of the line-of-sight velocity is drawn from a Gaussian distribution centered around the true line-of-sight velocity, with a standard deviation equal to the measurement uncertainty. In statistical terms, this is akin to saying that V_{los} is a random variable, Normally distributed with mean v_{los} and variance Δv_{los} :

$$V_{los} \sim \mathcal{N}(v_{los}, \Delta v_{los}) \quad (8)$$

(here standard statistical notation is used, where $\mathcal{N}(\mu, \sigma)$ represents the Normal distribution). With this assumption, the probability of obtaining a measurement v_{los} is

$$p(v_{los}|v_{los}, \Delta v_{los}) = \frac{1}{\sqrt{2\pi\Delta v_{los}^2}} e^{-\frac{(v_{los}-v_{los})^2}{2\Delta v_{los}^2}}. \quad (9)$$

The same Gaussian assumption is made for the probabilities of the other measurements $p(\mu_\delta|\mu_\delta, \Delta\mu_\delta)$, $p(\mu_\alpha \cos \delta|\mu_\alpha \cos \delta, \Delta\mu_\alpha \cos \delta)$, and $p(r|r, \Delta r)$. Because the kinematic measurements \mathbf{y} are made using independent methods, we assume that measurement errors are independent given the true values, so that the probability of measuring all components of a GC's kinematic quantities is simply the product of the probabilities defined above. Thus, the total likelihood is

$$\mathcal{L}(\mathbf{y}|\boldsymbol{\Delta}, \boldsymbol{\vartheta}) = p(r|r, \Delta r)p(v_{los}|v_{los}, \Delta v_{los}) \times p(\mu_\delta|\mu_\delta, \Delta\mu_\delta)p(\mu_\alpha \cos \delta|\mu_\alpha \cos \delta, \Delta\mu_\alpha \cos \delta) \quad (10)$$

(Eadie et al. 2015a,c). This defines our measurement model. We acknowledge that the measurements of the two components of the proper motion are not actually independent. Their correlation could be incorporated

using a multivariate normal, but because these correlations are not usually reported, we leave this to future work.

A similar hierarchical set-up was recently used by Fornasa & Green (2014) in a study that attempted to infer the velocity dispersion of local dark matter particles. In the Bayesian framework, they treated the position and velocity of the Sun as nuisance parameters; Gaussian distributions centered on the measured values and with variances determined by the uncertainties in the measurements were used to constrain the values of $(R_\odot, U_\odot, V_\odot, W_\odot)$. Our set-up differs from theirs in that we are using the Gaussian distributions as the likelihood for all of the data.

Equipped with an expression for the likelihood (Eq. 10), we next define prior distributions on the parameters. These prior distributions link the measurement model to the tracer/galactic mass model. The parameters $\boldsymbol{\vartheta}$ represent the true positions and velocities, and we assume that these parameters have a prior distribution defined by Equation 3. Because the DF has its own parameters $\boldsymbol{\theta}$, *hyperpriors* $p(\boldsymbol{\theta})$ must also be specified. Thus, for a single GC or tracer, Bayes' rule can be written as

$$p(\boldsymbol{\theta}|\mathbf{y}, \boldsymbol{\Delta}) \propto \mathcal{L}(\mathbf{y}|\boldsymbol{\Delta}, \boldsymbol{\vartheta}) \times p(h(\boldsymbol{\vartheta})|\boldsymbol{\theta}) \times p(\boldsymbol{\theta}) \\ \propto \text{Likelihood} \times \text{Prior} \times \text{Hyperprior}$$

where the function h is the transformation from Heliocentric to Galactocentric coordinates (Section 2.3). Assuming that the GCs are conditionally independent, the posterior distribution is proportional to

$$p(\boldsymbol{\theta}|\mathbf{y}, \boldsymbol{\Delta}) \propto \prod_i^N \mathcal{L}(\mathbf{y}_i|\boldsymbol{\vartheta}_i, \boldsymbol{\Delta}_i)p(h(\boldsymbol{\vartheta}_i)|\boldsymbol{\theta})p(\boldsymbol{\theta}). \quad (11)$$

The hierarchical Bayesian specification above provides a couple of improvements to Papers I and II (Equation 1). First and foremost, measurement uncertainties are included in the analysis. Second, whereas before only 89 of 157 GCs could be included¹, we can now include 143 GCs. The remaining 14 GCs are objects for which no measurements of velocity are known (see Table 4 in Eadie & Harris 2016).

2.2. Defining Priors and Hyperpriors

Defining priors in the Bayesian paradigm is an opportunity for the researcher to state their prior knowledge, gained from previous studies, and their prior assumptions about model parameters. For this study, we use the same prior distributions as Paper II for parameters Φ_\odot , γ , and β .

¹ Mainly due to the GCs' locations, see Papers I & II

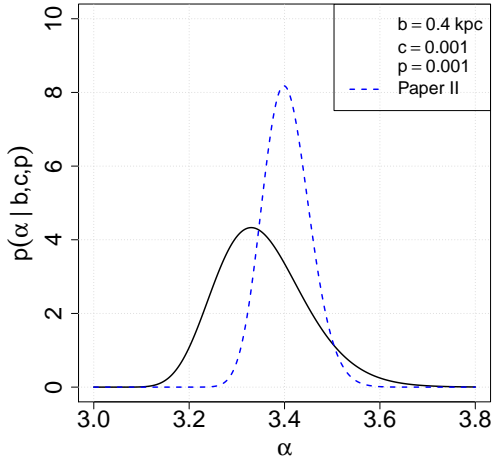


Figure 1. The solid black line is the prior distribution used in this paper, and the blue dashed line was the prior distribution used in Paper II. The solid-line prior probability distribution for α is determined using the extra GC data ($n = 14$) that is not used in the rest of the analysis. Thus, the prior used in this study is less informative than that used in Paper II.

The prior on the GC spatial distribution parameter, $p(\alpha)$, is a Gamma distribution. This choice was established and justified in Paper II, and was defined using the extra 68 GCs not otherwise included in the analysis. In this study, however, most of these previously excluded GCs can now be included because we do not have to depend on geometric assumptions to get v_{los} . However, there remain 14 GCs mentioned in Section 2.1 that are excluded because they have only position measurements. We use these 14 GC positions to estimate and define a prior distribution the parameter α , and compare the new $p(\alpha)$ to that used in Paper II (Figure 1). Note that the new prior is wider than the one used in Paper II, because fewer GCs were used to estimate and define it. Including the extra GC data in the prior is akin to including all of the positions of GCs in the analysis.

The priors for the parameters ϑ are given by the DF (Equation 3).

2.3. Transformation of Velocities

In this section we discuss the function $h(\vartheta)$ first mentioned in Section 2.1. The $h(\vartheta)$ notation symbolizes the transformation of velocity parameters in Eq. 5 from a Heliocentric parameterization ($r, v_{los}, \mu_\delta, \mu_\alpha \cos \delta$) to a Galactocentric parameterization (v_r, v_t), following the method presented in Johnson & Soderblom (1987). We present a brief review of the Johnson & Soderblom (1987) method here, in order to highlight some important points.

The first step is to transform the Heliocentric velocities into Galactic space-velocities (U, V, W) in a right-

handed coordinate system:

$$\begin{bmatrix} U \\ V \\ W \end{bmatrix} = \mathbf{T} \cdot \mathbf{A} \begin{bmatrix} \rho \\ k\mu_\alpha \cos(\delta) \\ k\mu_\delta \end{bmatrix} + \begin{bmatrix} U_\odot \\ V_\odot \\ W_\odot \end{bmatrix} \quad (12)$$

where U is positive towards the Galactic centre, V is positive in the direction of Galactic rotation, and W is positive above the Galactic plane. The solar motion is set to $(U_\odot, V_\odot, W_\odot) = (11.1, 12.24, 7.25)$ (Schönrich et al. 2010), and $k = 4.74057$. The matrices \mathbf{T} and \mathbf{A} depend on the right-ascension (RA) and declination (DEC) of the North Galactic Pole (as determined by the Hipparcos catalog) and GCs respectively. Specifically, \mathbf{A} for a single GC is

$$\mathbf{A} = \begin{bmatrix} +\cos \alpha \cos \delta & -\sin \alpha & -\cos \alpha \sin \delta \\ +\sin \alpha \cos \delta & +\cos \alpha & -\sin \alpha \sin \delta \\ +\sin \delta & 0 & +\cos \delta \end{bmatrix} \quad (13)$$

where α is RA and δ is DEC, in decimal degrees (this α is different from the one used to parameterize the GC distribution above). Note that if RA and DEC are treated as parameters in the hierarchical Bayesian framework, then Equation 13 would change for every GC, at every step of the Markov chain, and sampling of the posterior distribution becomes computationally prohibitive. Thus, for computational efficiency, we take the GCs' RA and DEC positions as fixed, and instead treat the Galactocentric distance r as a parameter in the model, and assign an uncertainty of 5% to the measured r value.

The next step is to transform the Cartesian, rotating Galactic frame velocity components (U, V, W) into components in a cylindrical, non-rotating Galactocentric reference frame (Π, Θ, W). First the adjustment for the rotation of the Galaxy at $R_\odot = 8.0\text{kpc}$ is taken to be 220km/s, to obtain (U_{gc}, V_{gc}, W_{gc}) , and then this vector is transformed to a non-rotating, right-handed cylindrical system via

$$\begin{bmatrix} \Pi \\ \Theta \\ Z \end{bmatrix} = \begin{bmatrix} \cos \theta & \sin \theta & 0 \\ -\sin \theta & \cos \theta & 0 \\ 0 & 0 & 1 \end{bmatrix} \begin{bmatrix} U_{gc} \\ V_{gc} \\ W_{gc} \end{bmatrix} \quad (14)$$

As a test of the entire transformation, we compare our derived (Π, Θ, W) to the Cassetti online catalog of GC measurements (Figure 2) (Dinescu et al. 1999, 2004, 2005; Cassetti-Dinescu et al. 2010, 2013)².

Finally, the velocity components in Eq. 14 are trans-

² Updated catalog: www.astro.yale.edu/dana/gc.html

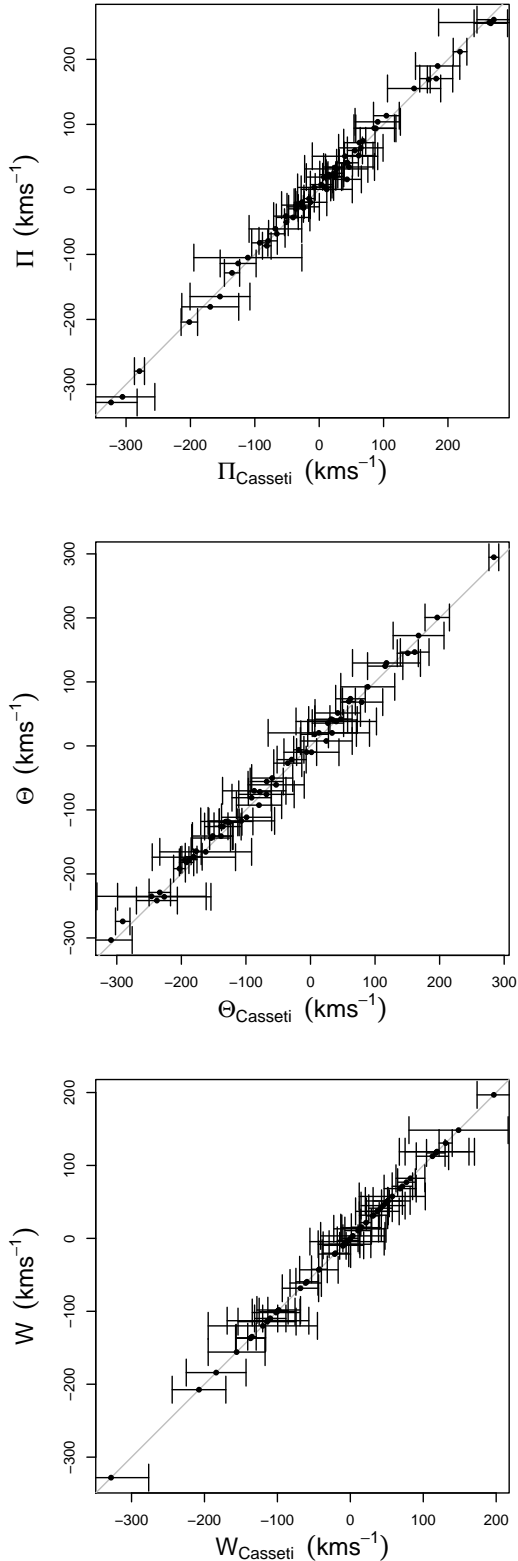


Figure 2. Velocity transformation. Our transformation from Heliocentric velocities to Galactocentric velocities (Θ, Π, W) for GCs with proper motions, compared to the Caseti catalog. The abscissa are from the Caseti online catalog, and the ordinates are our transformation values. The error bars are the uncertainties given in the Caseti catalog, and the grey line has a slope of one.

formed to the spherical coordinate system

$$\begin{bmatrix} v_r \\ v_\theta \\ v_\phi \end{bmatrix} = \begin{bmatrix} \cos \phi & 0 & \sin \phi \\ 0 & 1 & 0 \\ -\sin \phi & 0 & \cos \phi \end{bmatrix} \begin{bmatrix} \Pi \\ \Theta \\ W \end{bmatrix} \quad (15)$$

where $v_t^2 = v_\theta^2 + v_\phi^2$. To reiterate, the transformation from the Galactocentric parameterization to the Heliocentric parameterization described above is represented by $h(\vartheta)$ in Equation 3.

3. KINEMATIC DATA

The kinematic data used in this study is presented in Table 1 of Paper II. In Paper II, only 89 out of 157 GCs were used in the analysis, mainly because the approximation $|v_{los}| \approx |v_r|$ did not hold for most GCs without proper motions. Other GCs were excluded for various reasons (e.g. they were subject to high reddening and thus large uncertainties, had no velocity measurements, or were associated with the LMC).

As described in Section 2, using the hierarchical Bayesian framework allows all of the incomplete data to be included without having to make any geometric arguments like those used in Papers I and II. This increases the size of the data set significantly, from 89 to 143 GCs. Although there are 157 GCs listed in Table 1 of Paper II, 14 of these GCs do not have any velocity measurements and are excluded from the sample. Instead, these 14 GCs' r positions are used to constrain the prior on α (i.e. the solid black line in Figure 1).

In Paper II, some GCs were excluded from the analysis because their observations suffered from high reddening. Now that we are accounting for these large uncertainties with the hierarchical model, we include these clusters. In Paper II, other GCs were excluded because they are believed to be associated with the LMC. However, including these clusters in the present analysis does not change the result significantly and therefore we choose to include them.

To make a fair comparison between the non-hierarchical method of Paper II and the hierarchical method presented here, and to thereby directly test the influence of measurement uncertainties, we first apply the hierarchical Bayesian method to the same kinematic data that was analyzed in Paper II (i.e. only 89 GCs). In this case, we use the prior distribution $p(\alpha)$ for the tracer spatial parameter that was used in Paper II (i.e. shown as the dashed blue line in Figure 1).

4. RESULTS

Figure 3 compares the 95% Bayesian credible regions for the mass profiles of the Milky Way from Paper II (the dashed, black lines) to the 50%, 75%, and 95% regions from this paper (the shaded blue regions). Both results rely on the same 89 GC sample used in Paper II; the only difference between the two analyses is that measurement uncertainties are now included.

The sample size used in Paper II consisted of 89 GCs, and 71 of these had complete data. One advantage of the hierarchical model is that sample size is increased to 143 GCs, but the GC data that are added to the sample are incomplete. Figure 4 compares the hierarchical method when 89 GCs are used versus 143 GCs. The dashed, blue lines indicate the 95% Bayesian credible regions from Figure 3, and the black shaded regions indicate the credible regions when 143 GCs are included. Although the sample size increased by more than 60%, the *proportion* of GCs with complete data decreased to about 50%. The increase in total sample size likely accounts for the slight narrowing of the Bayesian credible regions. However, the difference between the hierarchical results from the 89 GC sample to the 143 GC sample is not as large as might be expected. It is our conjecture that a more constrained estimate using the present method will require a higher proportion of complete data.

The GCs are subject to the total gravitational potential within their orbits, and thus trace the total mass out to 125kpc. Using the hierarchical Bayesian method presented here, the power-law models, and the priors, and confronting this coherent model with the GC data returns a total mass within 125kpc of $4.81 \times 10^{11} M_{\odot}$, with a 95% credible region of $(3.96, 5.76) \times 10^{11} M_{\odot}$.

Extrapolating our mass profile in Figure 4 out to a virial radius that corresponds to 200 times the critical density of the universe, assuming $H_o = 67.8 \text{ km s}^{-1} \text{ Mpc}^{-1}$ (Planck Collaboration et al. 2015), we find that $r_{vir} = 179$ (174, 184) kpc and $M(r_{vir}) = 6.16(5.62, 6.66) \times 10^{11} M_{\odot}$ (numbers in brackets correspond to the 95% Bayesian credible regions). Extrapolating out further, the mass within 300 kpc is $M(300 \text{ kpc}) = 0.87(0.70, 1.05) \times 10^{12} M_{\odot}$.

In Paper II, we performed a sensitivity analysis to determine how the spatial sample of GCs might affect the mass estimate of the Milky Way under our assumed power-law model. The sensitivity analysis involved obtaining mass estimates after removing GCs with positions within five different r_{cut} values: 5, 10, 15, and 20 kpc. Here we repeat the same sensitivity analysis using the same set of r_{cut} values, but using the full sample of 143 GCs. In contrast to Paper II, we find that the mass estimate within 125 kpc is robust to the systematic exclusion of inner GCs, except perhaps when only

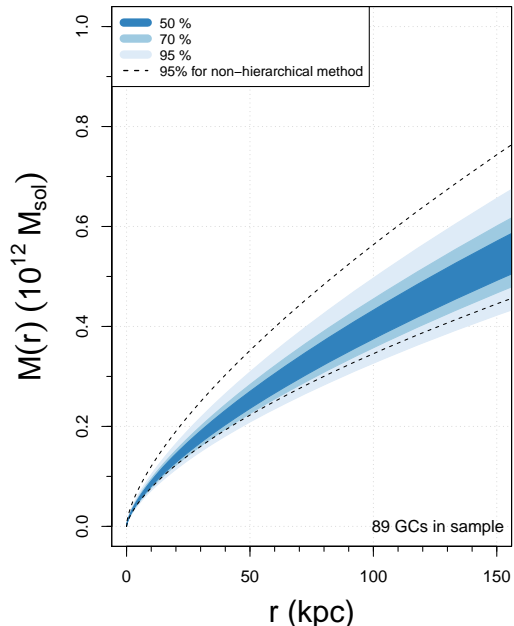


Figure 3. The blue shaded areas are the Bayesian credible regions for the cumulative mass profile of the Milky Way, using the hierarchical method and 89 GCs. The black dashed lines show the 95% credible regions for the non-hierarchical method and 89 GCs (i.e. the results from Paper II).

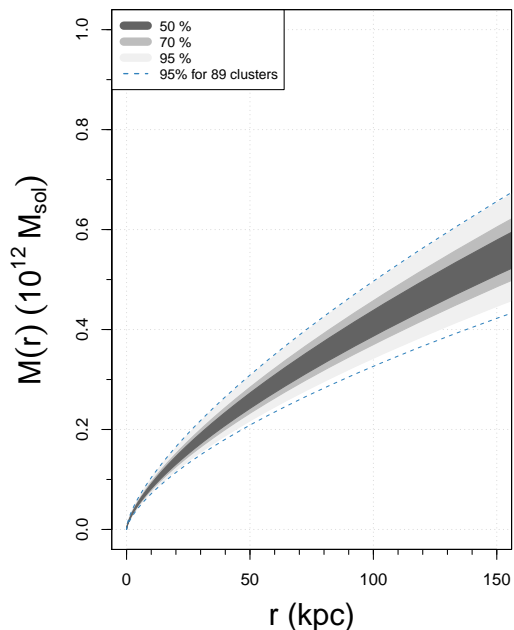


Figure 4. The grey shaded areas are the Bayesian credible regions for the cumulative mass profile of the Milky Way using the hierarchical method and 143 GCs. The blue dashed lines show the 95% credible regions for the hierarchical method and 89 GCs (i.e. the outermost blue region in Figure 3).

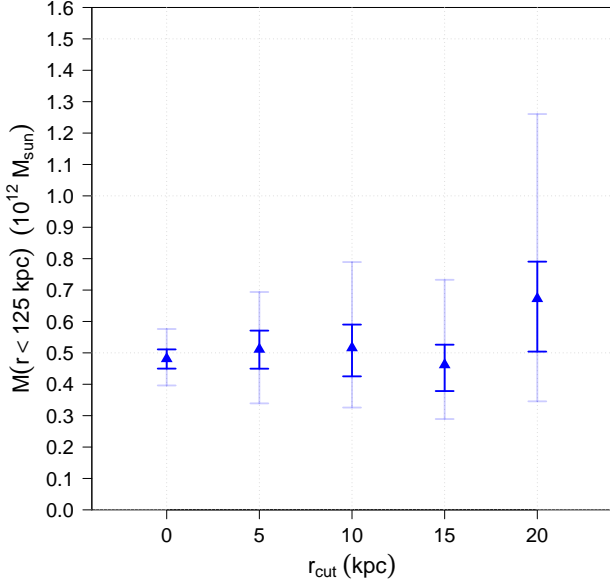


Figure 5. Sensitivity analysis: The estimate of the total mass within 125kpc (M_{125}) for different GC samples. GCs within the r_{cut} value are removed from the sample (for example, M_{125} at $r_{cut} = 10$ corresponds to mass estimate when GCs within 10kpc are removed from the sample). Inner bars are 50% credible regions and outer bars are 95% credible regions.

GCs beyond 20 kpc are used in the analysis (Figure 5). We note however that there are only 19 GCs beyond 20 kpc, and only 4 of these GCs have proper motion measurements. Accordingly, the uncertainty in the mass increases significantly in this case, and the 95% credible regions overlap with mass estimates under smaller r_{cut} values. These results suggest that the current model is adequate for describing the profile of GCs, at least with regard to estimating the total mass within 125kpc. If current tracer model was not properly specified, we would expect the mass estimate to change as inner tracers were systematically removed. We see no evidence of this occurring.

Figure 6 displays how the individual model parameters Φ_o , γ , α , and β vary in the sensitivity analysis. A positive correlation in the estimates of Φ_o and γ is immediately obvious in the upper two panels, and as more inner GCs are excluded (i.e. as r_{cut} increases) $\gamma \rightarrow 0.5$. This value of γ corresponds to an approximate Navarro et al. (1996) profile at large radii (Deason et al. 2011).

The parameter α , the power-law slope of the GC population, is highly constrained in the analysis, regardless of the GC sample that is used. One thing to note is that the prior $p(\alpha)$ becomes less and less informative for each r_{cut} , as the extra data available to define a prior goes from 14 GCs to 6, 5, and 3 GCs.

The β estimates in the sensitivity analysis are in good agreement with one another, despite the percentage of

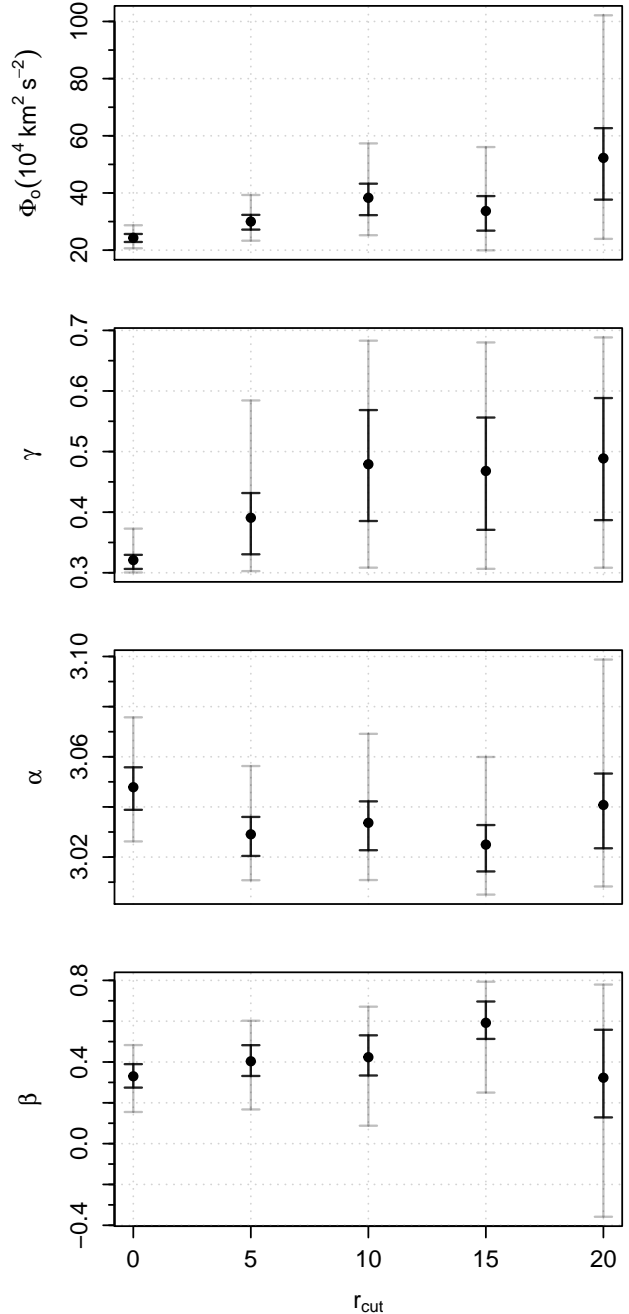


Figure 6. Sensitivity analysis: Parameter estimates when GCs within the r_{cut} value are removed from the sample. Inner bars are 50% credible regions and outer bars are 95% credible regions.

complete data decreasing as r_{cut} increases. We can therefore conclude that the GC population has a mildly radial constant anisotropy under this model assumption. However, when the GC sample is limited to clusters outside 20 kpc the uncertainty in β becomes quite large.

To summarize the entire posterior distribution for the full sample of 143 GCs, we show the joint credible regions for all four model parameters (Figure 7).

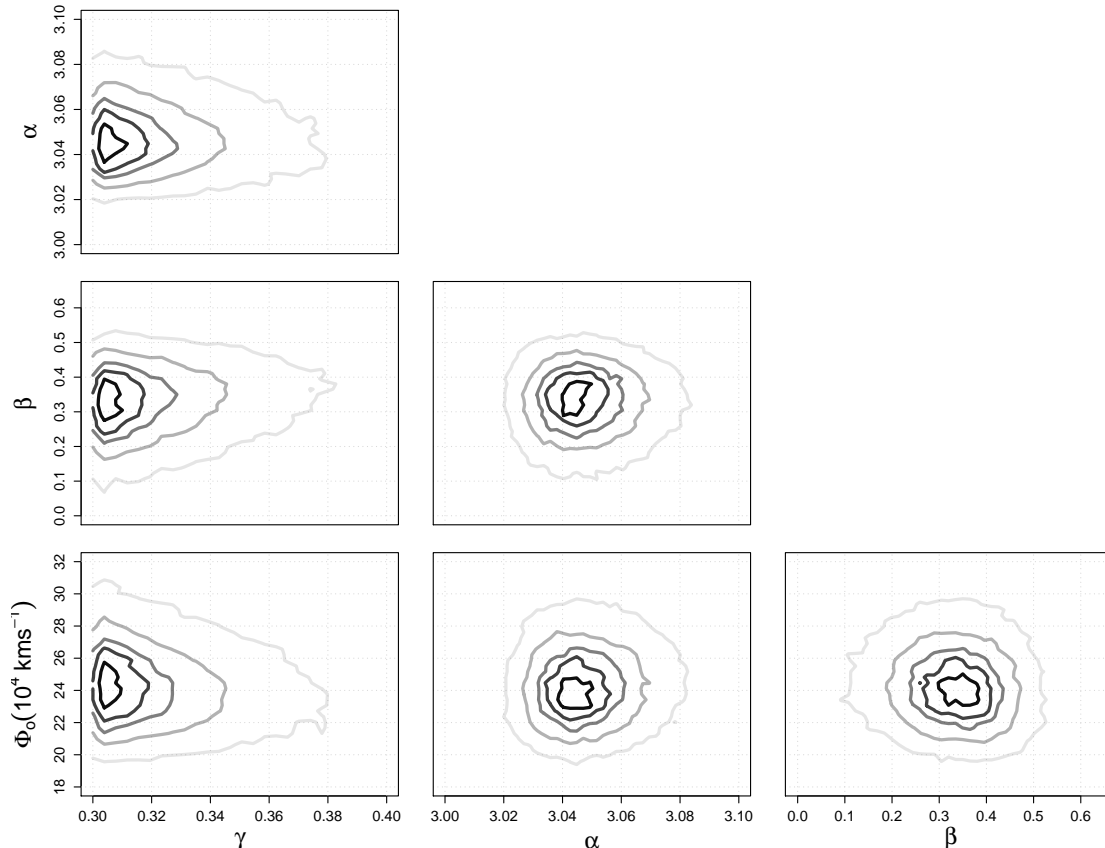


Figure 7. Joint posterior distributions for the model parameters. The curves show the 10%, 20%, 30%, 50%, 75%, and 95% Bayesian credible regions.

Because the hierarchical method treats the Heliocentric positions and velocities as parameters in the model, the final posterior distribution provides estimates and credible regions for the parameters $\vartheta = (r, v_{los}, \mu_\delta, \mu_\alpha \cos \delta)$ for all 143 GCs (i.e. there are 572 parameters in the GCs measurement model alone). Using the posterior distributions for these parameters, we can derive an estimate of the relative energy \mathcal{E} for each cluster, with credible regions. Figure 8 shows these energy estimates as a function of Galactocentric position: hollow and solid blue circles are the mean energy estimates of the incomplete and complete data parameters. The solid green diamonds show the energies derived from the measurements of the complete data (there are no hollow green diamonds because energies cannot be derived without proper motions). Arrows from the solid green diamonds to the solid blue points connect the same GC. For legibility, we do not show the 95% credible regions for the energies, but we have checked that the credible regions appear reasonable. The shaded purple curves enclose the 50% and 95% credible regions for the gravitational potential, determined pointwise as a function of r .

Figure 8 provides a consistency check to the hierarchi-

cal method in three ways: (1) the distribution of points is consistent with our initial assumptions that all GCs are bound to the Galaxy, (2) the incomplete and complete data energy distributions populate the region between the gravitational potential and the zero line, and (3) the incomplete and complete data do not appear to have different energy distributions. Another feature of note is the tendency for the estimated energies based on positions and velocities to be shrunk towards a curve similar in shape to the $\Phi(r)$ profile. This is because the posterior distributions for each tracer’s energy are in some sense a compromise between the prior implied by tracer model (Equation 3) and the measured value. Whether the posterior distribution is closer to the measured value or the value implied by the tracer model is a function of the width of the prior compared to the measurement uncertainty of the tracer.

5. DISCUSSION

The Bayesian method presented here has an advantage compared to traditional point mass estimation techniques in the literature because it uses complete and incomplete data simultaneously in the analysis, whereas other techniques use either complete or incomplete data

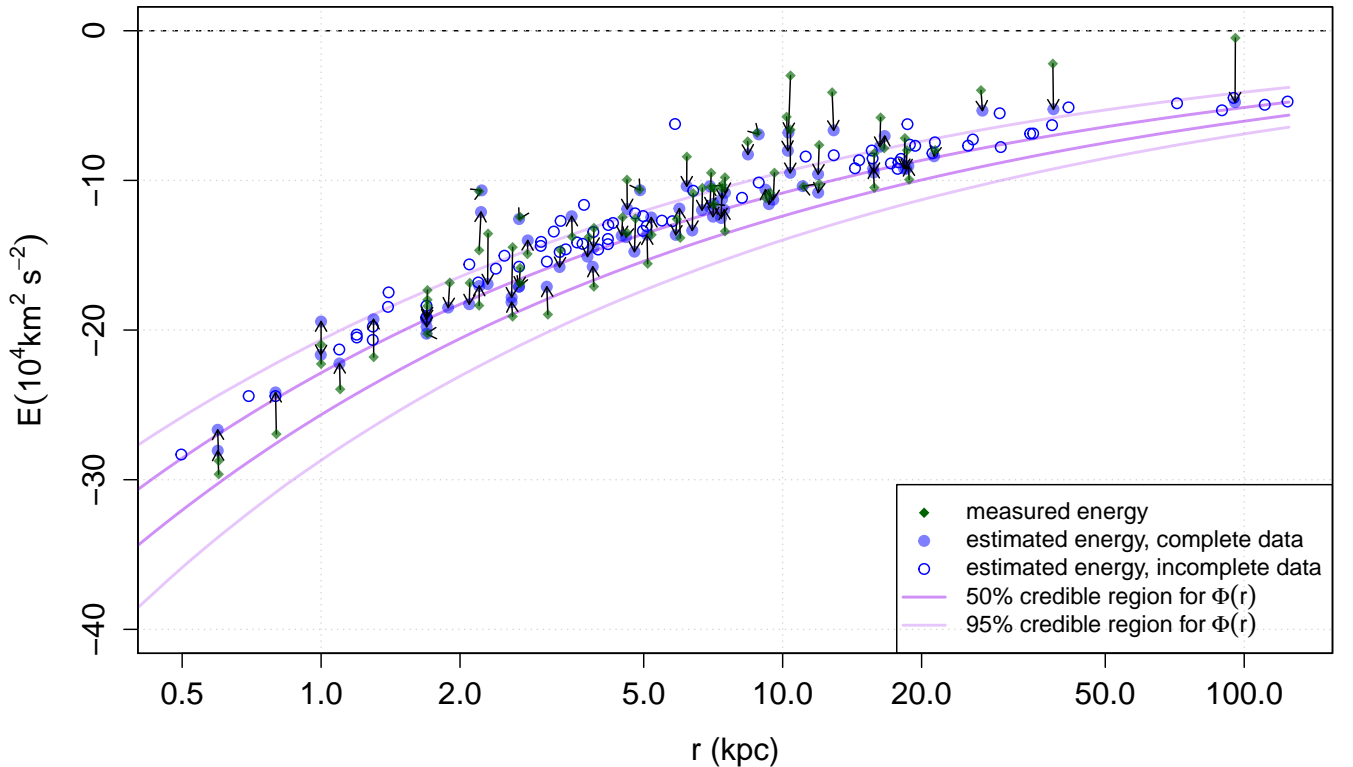


Figure 8. Specific energy estimates of GCs as a function of Galactocentric position. The blue circles are the mean energy estimates for each GC; solid points are complete data and hollow points are incomplete data. The solid green diamonds are the measured energies for complete data. The arrows connect GC measured energies to GC estimated energies, and the purple curves represent the 50 and 95% credible regions for the potential. Bound GCs lie between the zero line and the lower 95% gravitational potential curve.

only (e.g. the mass estimators introduced by Bahcall & Tremaine 1981; Evans et al. 2003; Watkins et al. 2010). Furthermore, although other studies have used a Bayesian analysis to infer the mass of the Milky Way (e.g. Little & Tremaine 1987; Kulesa & Lynden-Bell 1992; Kochanek 1996; Wilkinson & Evans 1999; McMillan 2011; Kafle et al. 2012; Williams & Evans 2015; Küpper et al. 2015), to our knowledge none of these studies has included measurement uncertainties using a coherent measurement model as we have done here.

Including the measurement uncertainties in a measurement model introduced four additional parameters for every GC, which increases the computational cost of the analysis. Nonetheless, even with 576 parameters (572 measurement model parameters ϑ and 4 tracer model parameters θ), we were able to run these analyses overnight on a personal computer with four cores after sufficient Markov chain burn-in.

We found that including uncertainties in the analysis resulted in a tighter constraint on the cumulative mass profile of the Milky Way compared to ignoring measurement uncertainties (Figure 3). This somewhat paradoxical result might be explained by attributing some of the

variation in GCs kinetics to the measurement process, as described in Figure 8. Without allowing for measurement error, the tracer model is made to explain all of the variation, which apparently results in increased overall uncertainty in the mass profile.

When the sample size of GCs went from 89 to 143, neither the value nor the spread of the mass profile changed much (Figure 4). Although introducing additional data might be expected to decrease the width of the Bayesian credible regions, this was not observed, and we suspect this is most likely due to a decrease in the proportion of complete measurements. When 143 GCs are included in the analysis, nearly 50% of the data are incomplete. In contrast, when the previous set of 89 GCs are included, almost 80% of the data are complete. We therefore stress the importance of having accurate, proper motion data for tracer objects.

In particular, there is a need for *remote* tracers with complete measurements. As shown by our sensitivity analysis (Figures 5 and 6), as inner GCs are removed from the sample, the percentage of incomplete data increases and this results in poorly constrained estimates of parameters and physical quantities such as enclosed

mass. The results of the sensitivity analysis, combined with the relatively unchanged result when we complete the analysis with 89 versus 143 clusters, lead us to the conclusion that it is absolutely critical to have proper motions for distant tracers.

An illuminating follow-up investigation to this study is to analyze simulations of Milky Way-type galaxies and their satellites using our hierarchical method. We are currently in the process of performing such analyses to determine how much proper motion data is necessary to constrain the mass profile further, and to also study what biases could occur under the Galaxy model that we have employed (Eadie, Keller, et al. in prep).

The mass profile result we have obtained in this study is at the lower end of most mass estimates in the literature, but is also in agreement with some more recent measurements (e.g. Deason et al. 2012a; Battaglia et al. 2005; Gibbons et al. 2014). Because the result obtained in this study is so similar to the mass profile of Paper II, we refer the reader to that paper for further comparison to other studies.

6. CONCLUSION

We have described a coherent, hierarchical Bayesian method for estimating the mass profile of the Milky Way galaxy, and applied this method to the Galaxy using GC data. This statistical framework allows us to take full advantage of all of the available GC kinematic data, and also provides a meaningful and coherent probabilistic way to incorporate measurement uncertainties.

Under the assumptions of the power-law model (Section 2.1), the hierarchical framework for including un-

certainties (Section 2), and the prior distributions (Section 2.2), and confronting this model with data from 143 GCs around the Milky Way, we arrive at a cumulative mass profile for the Galaxy with uncertainties (Figure 4) and a mass estimate within 125 kpc of $4.81 \times 10^{11} M_{\odot}$ (the 95% Bayesian credible regions are $(3.96 - 5.76) \times 10^{11} M_{\odot}$). When we extrapolate out the mass profile to the virial radius (≈ 179 kpc), we find $M_{vir} = 6.14 \times 10^{11} M_{\odot}$ with a 95% Bayesian credible region of $(5.64 - 6.67) \times 10^{11} M_{\odot}$. This mass estimate is notably lower than other studies.

The statistical framework presented here will be highly useful and appropriate for other tracer objects around the Milky Way, such as halo stars and dwarf galaxies. Using our approach with data sets from large programs such as Gaia could yield a well-constrained mass estimate for the Galaxy. Incorporating large data sets in this analysis will present some computational challenges, but given the effectiveness of our MCMC sampler we are confident that this will be a tractable problem through parallelization.

The first order of business, however, is to better understand what tracer populations will provide the most information about the Milky Way's gravitational potential. Thus, we are currently performing a blind-test of simulated data of Milky Way-type galaxies that were created through hydrodynamical simulations.

WEH and GME acknowledge the financial support of NSERC and McMaster University.

REFERENCES

- Bahcall, J. N., & Tremaine, S. 1981, *The Astrophysical Journal*, 244, 805
- Battaglia, G., Helmi, A., Morrison, H., et al. 2005, *MNRAS*, 364, 433
- Binney, J., & Tremaine, S. 2008, *Galactic Dynamics*, 2nd edn. (Princeton)
- Casetti-Dinescu, D. I., Girard, T. M., Jílková, L., et al. 2013, *AJ*, 146, 33
- Casetti-Dinescu, D. I., Girard, T. M., Korchagin, V. I., van Altena, W. F., & López, C. E. 2010, *AJ*, 140, 1282
- Deason, A. J., Belokurov, V., & Evans, N. W. 2011, *MNRAS*, 411, 1480
- Deason, A. J., Belokurov, V., Evans, N. W., & An, J. 2012a, *MNRAS*, 424, L44
- Deason, A. J., Belokurov, V., Evans, N. W., & McCarthy, I. G. 2012b, *ApJ*, 748, 2
- Dinescu, D. I., Girard, T. M., & van Altena, W. F. 1999, *AJ*, 117, 1792
- Dinescu, D. I., Keeney, B. A., Majewski, S. R., & Girard, T. M. 2004, *AJ*, 128, 687
- Dinescu, D. I., Martínez-Delgado, D., Girard, T. M., et al. 2005, *ApJL*, 631, L49
- Eadie, G., Harris, W., & Springford, A. 2015a, in *Joint Statistical Meetings Proceedings (American Statistical Association)*
- Eadie, G. M., & Harris, W. E. 2016, *ApJ*, 9999, 9999
- Eadie, G. M., Harris, W. E., & Widrow, L. M. 2015b, *ApJ*, 806, 54
- Eadie, G. M., Harris, W. E., Widrow, L. M., & Springford, A. 2015c, in *Proceedings of the International Astronomical Union*, ed. A. Bragaglia, M. Arnaboldi, M. Rejkuba, & D. Romano (Cambridge Journals)
- Evans, N. W., Hafner, R. M., & de Zeeuw, P. T. 1997, *MNRAS*, 286, 315
- Evans, N. W., Wilkinson, M. I., Perrett, K. M., & Bridges, T. M. 2003, *The Astrophysical Journal*, 583, 752
- Fornasa, M., & Green, A. M. 2014, *PhRvD*, 89, 063531
- Gibbons, S. L. J., Belokurov, V., & Evans, N. W. 2014, *MNRAS*, 445, 3788
- Johnson, D. R. H., & Soderblom, D. R. 1987, *The Astronomical Journal*, 93, 864
- Kaffe, P. R., Sharma, S., Lewis, G. F., & Bland-Hawthorn, J. 2012, *ApJ*, 761, 98
- Kochanek, C. S. 1996, *The Astrophysical Journal*, 457, 228
- Kulassa, A. S., & Lynden-Bell, D. 1992, *MNRAS*, 255, 105

- Küpper, A. H. W., Balbinot, E., Bonaca, A., et al. 2015, *ApJ*, 803, 80
- Little, B., & Tremaine, S. 1987, *The Astrophysical Journal*, 320, 493
- McMillan, P. J. 2011, *MNRAS*, 414, 2446
- Navarro, J. F., Frenk, C. S., & White, S. D. M. 1996, *The Astrophysical Journal*, 462, 563
- Planck Collaboration, Ade, P. A. R., Aghanim, N., et al. 2015, *ArXiv e-prints*, arXiv:1502.01589
- Schönrich, R., Binney, J., & Dehnen, W. 2010, *MNRAS*, 403, 1829
- Wang, W., Han, J., Cooper, A., et al. 2015, *MNRAS*, 453, 377
- Watkins, L., Evans, N., & An, J. 2010, *MNRAS*, 406, 264
- Wilkinson, M., & Evans, N. 1999, *MNRAS*, 310
- Williams, A. A., & Evans, N. W. 2015, *MNRAS*, 454, 698